Materials & Design 267 (2026) 116270

Contents lists available at ScienceDirect

Materials & Design

journal homepage: www.elsevier.com/locate/matdes

On the microstructural strategies adopted for achieving improved machinability in commercial brass alloys

Erfan Sharghivand [a], Luca Bazzana [b], Antonio Costetti [a], Nino Mori [b], Massimiliano Annoni [a], Maurizio Vedani [a,*]

[a] *Politecnico di Milano, Department of Mechanical Engineering, 20156 Milan, Italy*
[b] *S.A. Eredi Gnutti Metalli SpA EGM, 25124 Brescia, Italy*

ARTICLE INFO

Keywords:
Brass alloys
Microstructure
Machinability
Si-bearing brass
Mg-bearing brass

ABSTRACT

Commercially available lead-free brasses with improved machinability were investigated to elucidate the microstructural mechanisms responsible for their enhanced interrupted chip formation. The study examines the microstructure and chip characteristics of alloys belonging to the Cu–Zn–Si (CW724R) and Cu–Zn–Mg (CW732R) lead-free systems and compares them with the standard CuZn42 (CW510L) and CuZn39Pb3 (CW614N) brasses. The results indicate that improved machinability in these lead-free alloys is achieved either by increasing the amount and hardness of the β phase through precipitation strengthening, as in the Mg-bearing CW732R alloy, or by promoting the formation of hard constituents capable of replacing the β phase, as observed in the Si-bearing CW724R alloy. Chip analyses from rough and fine turning tests revealed that CW724R develops a deformed chip microstructure characterized by periodic deep cracks and localized shear bands traversing the entire chip thickness, resulting in a discontinuous morphology comparable to that of the lead-bearing CW614N alloy. In contrast, the Mg-bearing CW732R alloy, despite its higher hardness and larger β phase fraction, displayed a chip morphology similar to the standard lead-free CW510L alloy under the machining conditions adopted here. These findings appear to contradict earlier reports showing superior machinability in similar Mg-bearing brasses, highlighting that the microstructural design of free-machining alloys must be carefully tailored to the specific chip-removal technology and machining parameters.

1. Introduction

Cu-Zn alloys (brasses) are used in a wide range of industrial sectors owing to their good corrosion resistance, machinability, plastic formability during forging and extrusion, non-magnetism, and low friction, paired with good mechanical properties. Typical applications include plumbing and electrical fittings, architectural hardware, decorative items, and various machined parts like screws, gears, and bearings.

Lead has been considered for decades as the reference element added to brass to ensure improved machinability. Owing to the low melting point (327,5°C) and complete immiscibility into copper, a dispersion of globular Pb particles is formed at grain boundaries of the brass matrix which exerts a twofold action: as a stress-raiser spot promoting chip fracture, resulting in the formation of small discontinuous chips, and as a lubricant for the chip surface that slides along the face of the cutting tool [1,2].

The effects of Pb in brasses have been the subject of a large number of investigations. There is full consensus about the importance of achieving a homogeneous dispersion of fine (less than 5 μm) Pb particles to promote an efficient chip breaking action [3,4]. It is known that Pb tends to collect mainly at α/β interphase boundaries assuming a spherical shape at the liquid stage to reduce surface energy [5]. The optimal amount of Pb for best machinability lays in the range 2.5–3.5 wt%, while an increased content may lead to surface cracking during hot working due to hot shortness [1]. In a recent study, Johansson and co-workers [2] compared the machining behaviour of a CuZn38Pb3 alloy with a lead-free counterpart CuZn42 alloy featuring comparable mechanical properties. They were able to demonstrate that the main action of Pb consists in promoting initiation sites for crack nucleation of the chip at the primary deformation zone, leading to discontinuous chip formation during machining. The lubrication effect expected by smearing of Pb on the tool rake surface was indeed not so prominent, since Pb was almost absent

---

* Corresponding author at: Politecnico di Milano, Department of Mechanical Engineering, Via Giuseppe La Masa, 1 - 20156 Milan, Italy.
E-mail addresses: erfan.sharghivand@polimi.it (E. Sharghivand), l.bazzana@eredignutti.it (L. Bazzana), antonio.castetti@polimi.it (A. Costetti), n.mori@eredignutti.it (N. Mori), massimiliano.annoni@polimi.it (M. Annoni), maurizio.vedani@polimi.it (M. Vedani).

https://doi.org/10.1016/j.matdes.2026.116270
Received 12 February 2026; Received in revised form 19 May 2026; Accepted 20 May 2026

from the theoretical contact area at tool tip (corresponding to the sliding region), while it was mainly found downstream, supposedly due to rubbing of chips after separation from the workpiece.

Pb is a heavily regulated element due to health and environmental concerns, especially for plumbing applications where, due to leaching and corrosion, it can be transferred into potable water [6,7]. Therefore, the development of lead-free brasses became a key research topic in last times to ensure compliance with progressively more stringent regulatory standards (see for instance ref. [8] for US regulations).

Efforts have been made into incorporating or promoting the formation of alternative soft second-phase particles in the microstructure of brasses to reproduce the effects of Pb for improved machinability. Bismuth was considered as a first "green" heavy metal candidate which can replace Pb owing to a similar low melting point and lack of solubility into Cu. Suksongkarm and co-workers proposed the addition of Bi-Sn obtained from recycled solder alloys to modify Cu-Zn-Si brass [9,10]. When added with a mass fraction of 2–4%, the 52Bi-48Sn dopant was able to generate a homogeneous dispersion of globular phases mainly embedded in the α phase of the brass matrix, which could prevent hot shortness phenomena due to the formation of low-melting films of Sn at grain boundaries, otherwise detected in simple Cu-Zn-Sn alloys. Machinability tests demonstrated that the chip shape shifted from a long continuous type to a more convenient discontinuous shape when adding 3 wt% of the Bi-Sn alloy to a Cu-38Zn0.5Si brass [10].

Researchers have also investigated experimental lead-free brasses incorporating Ti [11], P [12,13], graphite [14], molybdenum disulfide (MoS_2) [15], Si [12,13,16–20], Mg [21–23], and Sb [22], as also summarized in the review paper by Stavroulakis and co-workers [1]. From these studies it can be inferred that an alternative strategy to the formation of soft second-phase particles consists in increasing the amount of β phase and its hardness to promote chip breaking effects during machining. According to cutting theory, a moderate hardness difference between alloy constituents can produce an inhomogeneous microstructure that promotes the formation of discontinuous serrated chips and enhances alloy strength. However, when the hardness gap exceeds a critical threshold, machining costs increase due to accelerated tool wear [12,18].

Si has been extensively investigated as an additive for this purpose. Nobel and co-authors compared the microstructure and machinability of several brass alloys including a Si-bearing CW724R alloy [16]. Due to the lower amount of Zn (21 wt%) and the additional Si (3,4 wt%), this alloy showed a high fraction of α phase (60 vol%) and the presence of a hard Si-rich K phase along with γ-phase particles segregated at α grain boundaries. Compared with other investigated lead-free brasses, this alloy exhibited higher strength and improved machinability, reflected in better chip breakage, lower cutting forces, and reduced tool temperature, though at the cost of increased tool wear due to the presence of the hard phases. Taha and co-authors systematically investigated cast samples of lead-free brasses with Si contents ranging from 1 to 4 wt% [17,20]. By progressively increasing the amount of Si, the fraction of β phase initially increased replacing the α phase. With Si additions exceeding 2 wt%, the fraction of β rapidly decreased while γ phase and other brittle intermetallics appeared. Consistently, the chip type changed from continuous to discontinuous type and the cutting force was reduced, but the tool wear increased by 140% as Si was increased from 0 to 4 wt%. Si has also been used in combination with Al [18], Sb [22], and their mixtures [10]. Si and Al can both promote a substantial leftward shift of the β- and γ-fields in the Cu-Zn phase diagram. Additionally, Al can prevent Zn volatilization during casting by forming an Al_2O_3 film on melt surface [18]. The combination with Sb (up to 1,5 wt %) would further increase the presence of δ phase particles located at the interior and at boundaries of the β islands, providing an efficient strengthening effect [24]. Consistent findings on the role of Sb have been reported in [22] for Cu35ZnSb alloys with Sb contents ranging from 0 to 2.34 wt%. The addition of Sb refined the microstructure and promoted the precipitation of hard intermetallic particles, which reduced the toughness and ductility of the alloys. These changes improved machinability by lowering cutting forces, decreasing energy consumption, and altering chip morphology, albeit at the expense of increased abrasiveness and accelerated tool wear.

Finally, the effect of Mg on properties of brasses was investigated by Atsumi and co-authors [21]. Cu40ZnMg alloys containing from 0 to 1.5 wt% Mg were fabricated by spark plasma sintering (SPS), followed by solution treatment and extrusion. Increasing the Mg content promoted the formation of an α–β duplex structure with a higher fraction of β phase. In addition, fine $Mg(Cu,Zn)_2$ intermetallics precipitated during slow cooling after extrusion, contributing to grain refinement and, ultimately, enhancing tensile strength. Data about machinability for Cu35ZnMg alloys with Mg contents ranging from 0 to 1.79 wt% are available from the paper of Adineh and co-authors [22]. Similarly to Sb, Mg was found to improve the machinability of the investigated alloys. The sample containing 1,79 wt% of Mg showed the lowest cutting force and best chip morphology.

To anticipate the progressively stringent regulatory standards, several lead-free brasses with improved machinability have been proposed on the market in recent years. However, limited scientific information has been made available in the open literature so far on their microstructure-related mechanisms inducing the claimed machinability. It is therefore the aim of this paper to provide a significant insight into the microstructural design and machining performance of free-cutting brass alloys. Thus, the investigation will be based on the performance of commercial alloys belonging to the Cu-Zn-Si (CW724R) and Cu-Zn-Mg (CW732R) lead-free alloy systems, to be compared with conventionally-used CuZn42 (CW510L) and CuZn39Pb3 (CW614N) brasses.

2. Materials and experimental procedures

Several alloys in the form of commercially available extruded bars with diameter of 18 mm have been investigated. The chemical composition of the materials, measured by a Bruker Q4 Tasman spark Optical Emission Spectrometer (OES), is reported in Table 1. The phase stability of the alloys was theoretically evaluated based on the measured compositions, using the Thermo-Calc® software, relying on the TCCU6 v6.2 database for Cu alloys.

Sample preparation for microstructural analysis involved mounting longitudinally sectioned bar samples in epoxy resin, followed by grinding with SiC abrasive papers up to 2000 grit and subsequent polishing with 3 μm and 1 μm diamond suspensions. Metallographic etching was performed using a solution consisting of 1 g $FeCl_3$, 25 ml HCl, and 70 ml distilled water.

The microstructure of the extruded alloys was initially examined by optical microscopy using a Nikon Eclipse LV150NL light optical microscope. For more detailed characterization, a Zeiss Sigma 500 field-emission scanning electron microscope (SEM) was used, equipped with Oxford Instruments Ultim Max EDS detector for energy-dispersive X-ray spectrometry (EDS) and an Oxford Instruments C-Nano electron backscatter diffraction (EBSD) detector for phase identification, and for crystallographic orientation analysis.

Vickers hardness and microhardness measurements were performed to evaluate the bulk hardness of the alloys and the hardness of their individual phases, respectively. Tests were performed with loads of 2000 g and 10 g, using a dwell time of 15 s, on polished and slightly etched samples. For each condition, the resulting microhardness value was the average of at least five measurements.

Comparative machinability tests on the investigated alloys were performed on a Haas Automation CNC lathe (model TL-1HE) under dry cutting conditions, using TCGT 16T304F-AL carbide cutting inserts. These inserts are suitable for non-ferrous materials and are characterized by nose radius of 0.4 mm, rake angle of 20° and clearance angle of 7°. Two distinct machining setups were adopted to reproduce typical roughing and finishing turning operations, with the cutting parameters

Table 1
Chemical compositions (in weight %) of the alloys investigated.

Alloy	Cu	Pb	Sn	Fe	Si	P	Mg	Zn
CW510L / CuZn42	57.99	0.12	0.24	0.13				41.53
CW614N / CuZn39Pb3	58.60	2.39	0.26	0.30				38.46
CW732R / CuZn41Mg	58.33	0.06	0.05	0.12			0.46	41.10
CW724R / CuZn21Si3P	75.77	0.06		0.15	3.22	0.05		20.82

summarized in Table 2. These parameters have been selected according to the tool manufacturer indications, without considering any adjustment for each specific alloy. The cutting speed reported in Table 2 refers to the diameter of 17.9 mm, as 0.1 mm were preliminarily removed to avoid any effects of surface oxidation or contamination. Each cutting edge was employed for less than 10 s of machining time, to eliminate effects of progressive tool wear on results. During the tests, the chips generated were collected for subsequent analyses. Specifically, the chips produced under all tested conditions were examined in terms of their morphology and deformed microstructure by means of SEM and optical microscopy performed on sectioned samples.

Roughness measurements of the turned surfaces were carried out with an optical coordinate-measuring system Bruker Alicona μCMM. The central area of each specimen was considered for the analyses, applying a cut-off wavelength of 2500 μm.

3. Results and discussion

3.1. Phase composition

Simulations carried out to define expected phases in the investigated alloys under equilibrium are summarized in Fig. 1. For each alloy, the plot on left column shows the evolution of the main constituents with temperature, whereas the plot on the right depicts the formation of secondary phases on a magnified scale. The CW510L alloy represents a standard Cu-Zn binary brass. Upon solidification (Fig. 1a), the primary BCC β phase is first formed, followed by the partial solid-state transformation into FCC α phase. It must be clarified that the predicted fractions of α and β phases at low temperature (e.g. around 25 vol% of α phase and 75 vol% of β phase at room temperature) strictly refers to the achievement of equilibrium conditions, that can hardly be met under real conditions. Secondary phases mainly consist in Fe- and Fe-Sn rich intermetallics and in the residual Pb included in the alloy composition.

Alloy CW614N shows a similar phase evolution with temperature (Fig. 1b) with the only difference given by the presence of a much higher amount of the low melting Pb, which separates from the solidified Cu-rich matrix and shifts to solid state only at temperature as low as 327,5°C.

The Mg-bearing CW732R alloy features a substantially similar behaviour of the main phases (Fig. 1c) with the additional precipitation of the C15 Laves phase $Mg(Cu,Zn)_2$ starting from 640°C on cooling, and of $(Cu,Zn)_2P$ phase right from the liquid phase.

When compared to previous materials, the CW724R alloy features a significantly lower amount of Zn (20 wt%) and the presence of Si (3,2 wt %). This latter is a strong β-stabilizer element and the combined action of Si and Zn can be theoretically evaluated considering the Zinc equivalent parameter given by equation 1 [15,18].

Table 2
External turning parameters adopted for the machinability tests of the investigated alloys.

	Spindle revolution speed (rpm)	Cutting speed (m/min)	Feed (mm/rev)	Depth of cut (mm)
Roughing	2000	112.5	0.2	1
Finishing	2000	112.5	0.1	0.3

$$Zn_{eq} = \frac{C_{Zn} + \sum K_i C_i}{C_{Zn} + C_{Cu} + \sum K_i C_i} \bullet 100 \tag{1}$$

Being C_{Zn} and C_{Cu} the actual Zn and Cu contents in the alloy, and $\Sigma K_i C_i$ the sum of the products of the fraction of i-element (C_i) times its specific coefficient (K_i). K_i takes the values of 10, 6 and 2 for Si, Al and Sn, respectively. For the investigated CW724R alloy, the Zn_{eq} value can therefore be estimated as 63.5%, suggesting the presence of γ phase. A more detailed evaluation provided by the present simulation suggests that the room temperature microstructure is made of α phase together with a significant fraction of γ phase and a reduced amount of FeP_2 (Fig. 1d). It is also to remark that the simulation would suggest the presence at high temperature (till around 400°C) of a HCP phase with composition roughly corresponding to $Cu_2(Zn,Si)$, whose residual presence at room temperature is reasonably expected when the alloy is cooled under non-equilibrium conditions. In Si-bearing brasses, this HCP phase is identified as the K phase [19].

3.2. Microstructure

A collection of representative optical micrographs of the alloys investigated is reported in Fig. 2. At low magnifications, the CW510L and CW614N alloys (Fig. 2a and 2b) reveal the duplex α + β phase structure (being β the darker phase in these optical micrographs). The CW732R alloy still features a duplex α + β microstructure, with the additional presence of tiny precipitates within the β islands, as depicted in Fig. 2c. More detailed information about the microstructure of the CW732R alloy are collected in Fig. 3. The EBSD phase map and the inverse pole figure suggest the preferential position of the α phase at the boundaries of the primary β regions as isolated grains, or as plates growing within β grains. The SEM images reported in Fig. 3c and 3d paired with EDS microanalyses confirm the extensive precipitation of submicrometric particles rich in Mg, Cu and Zn within the β grains, that are assumed to match the $Mg(Cu,Zn)_2$ phase reported by the Thermo-Calc analyses.

Finally, the CW724R alloy shows a complex multi-phase structure (Fig. 2d). EBSD results reported in Fig. 4a and 4b reveal the presence of alternate and elongated islands containing grains of the FCC and HCP crystal structure. Based on local compositions detected by EDS and on suggestions provided by ThermoCalc results, these islands can be recognized as being made of α and K phases, respectively. Specifically, the Si-rich K phase would correspond to the nominal atomic composition Cu_8Zn_2Si [19]. SEM observations (Fig. 4c and 4d) linked with EDS analyses, highlighted more clearly the presence of a third phase with cubic crystal structure segregated at a grain boundaries, corresponding to the γ phase, in good agreement with other published research works [16,19].

The hardness and the associated abrasiveness of the investigated alloys are key properties that provide valuable insights into the relationship between microstructural features and cutting performance. It has already been highlighted that a moderate hardness difference between alloy constituents can promote the formation of discontinuous serrated chips during machining, whereas an excessive hardness difference tends to increase abrasiveness, leading to accelerated tool wear [12,18]. The abrasiveness of multiphase alloys toward cutting tools has been quantified using equation 2, where W_{ab} is the abrasiveness parameter, H is the average alloy hardness, V_2 is the volume fraction of the hardest phase, and H_2 and H_1 denote the hardness values of the

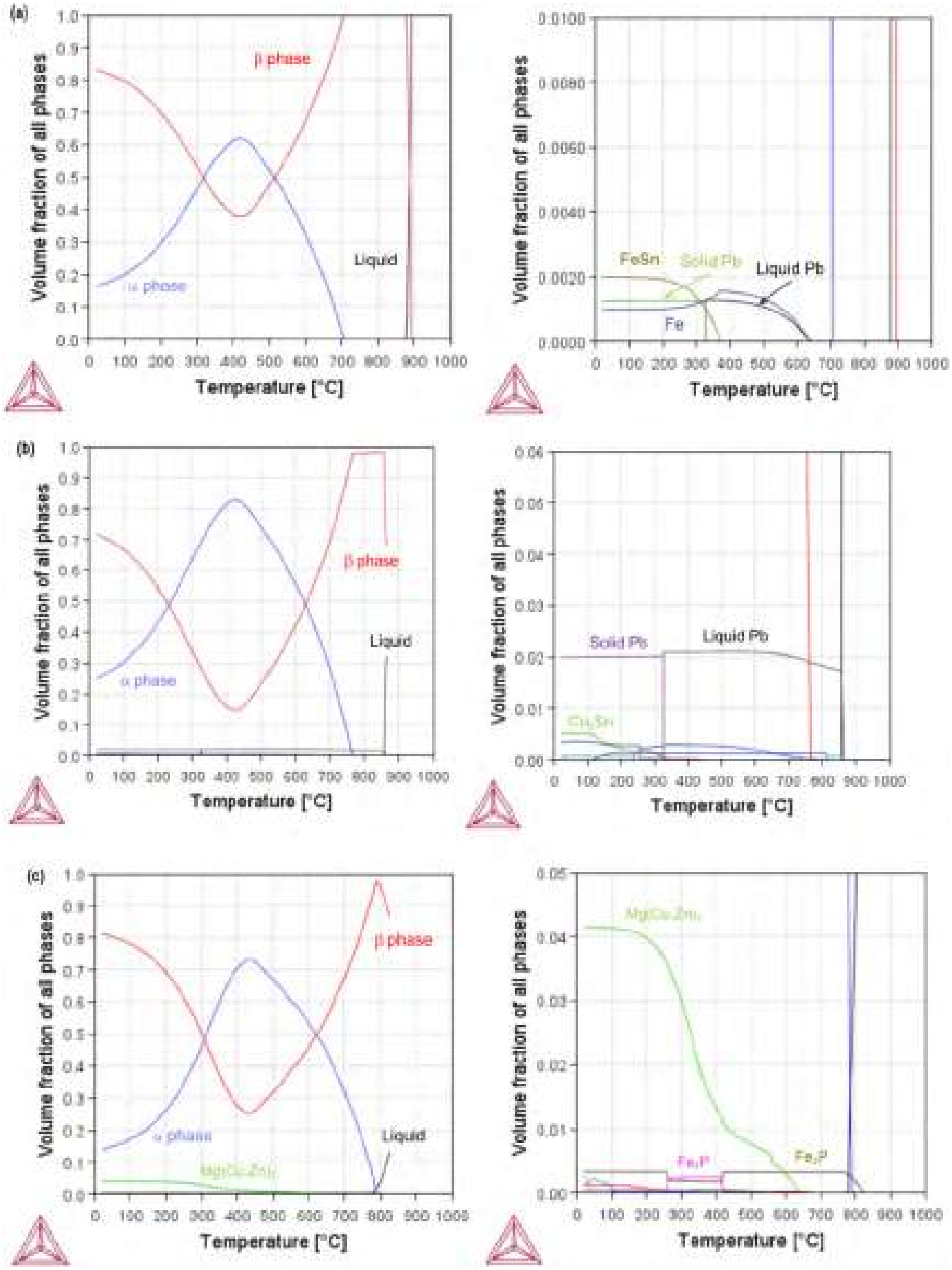

Fig. 1. *Phases expected in the investigated alloys under the hypothesis of equilibrium conditions; (a) CW510L alloy; (b) CW614N alloy, (c)* CW732R *alloy, (d) CW724R alloy.*

harder and softer phases, respectively [12,22].

$$W_{ab} = H + V_2 \cdot (H_2 - H_1) \tag{2}$$

Besides, it must be considered that for the assessment of the CW724R alloy abrasiveness, the effects of both the K and the γ hard phases must be considered. Therefore, a modification of equation 2 was here proposed (see equation 3) where V_3 and H_3 are the volume fraction and the hardness of the additional hard phase, respectively.

$$W_{ab} = H + V_2 \cdot (H_2 - H_1) + V_3 \cdot (H_3 - H_1) \tag{2}$$

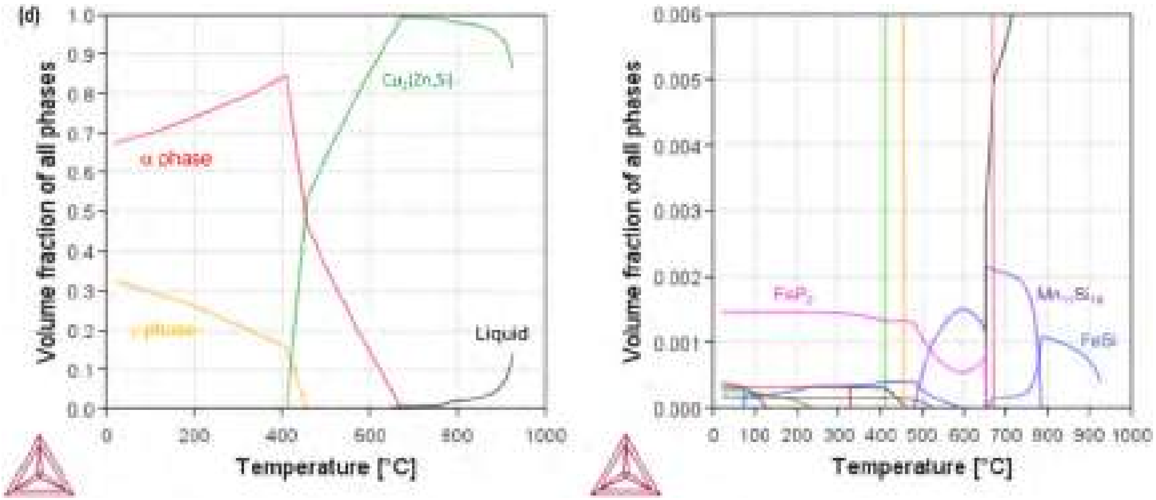

Fig. 1. (*continued*).

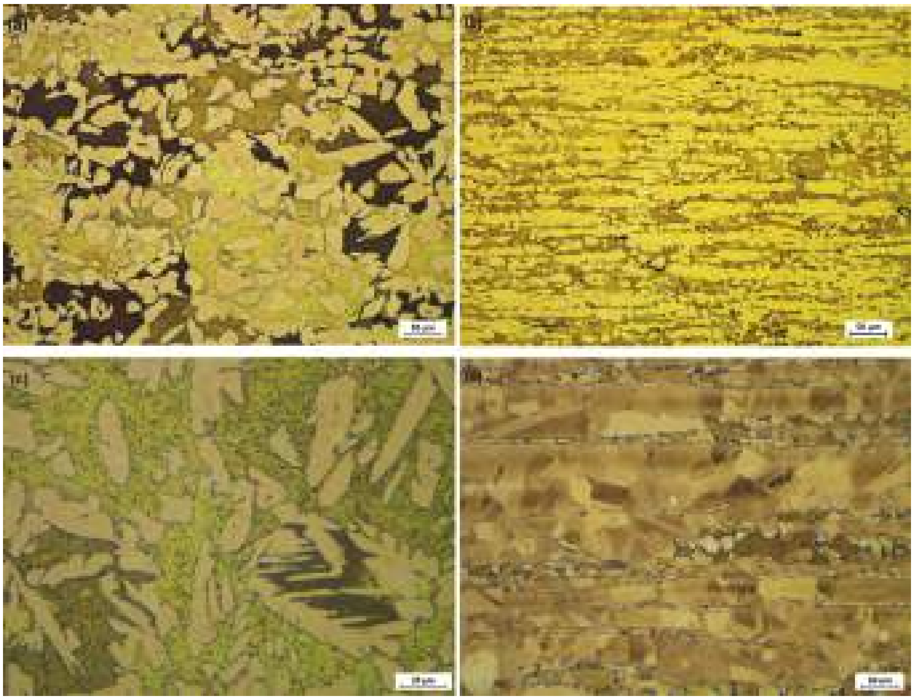

Fig. 2. Optical micrographs of the investigated alloys; (a) CW510L alloy; (b) CW614N alloy, (c) CW732R alloy, (d) CW724R alloy. Bar axes correspond to horizontal direction in all images.

Table 3 summarizes the collected hardness and microhardness data of individual phases, along with the evaluated abrasiveness index for the alloys investigated. The lowest abrasiveness is recorded for the softest lead-bearing CW614N alloy while higher values are estimated for the Mg-bearing CW732R and Si-bearing CW724R alloys owing to their higher bulk hardness and the contribution of the most abundant β phase and harder K and γ phases, respectively.

3.3. *Machining tests*

The evaluation of chip morphology offers valuable clues about the chip-formation mechanisms, and ultimately about alloy machinability for the specific turning conditions investigated. Figs. 5 and 6 depict representative images of the chips collected after testing the investigated alloys under roughing and finishing conditions, respectively. The higher depth of cut and feed adopted for the first set of turned samples led, for the CW510L and CW732R alloys, to thicker and curled chips, of the semi-continuous type, featuring a straight shape and periodic interruptions when reaching a length of around 100 mm. Instead, fully discontinuous chips were produced when roughing the CW614N and CW724R alloys, the former with tight helical shape that approached a tubular aspect a few dozens of mm in length, the latter showing more opened and shorter fragments. Higher-magnification side views of the chips taken by SEM highlight the periodic shear planes generated during cutting, separated by a distance of around 100 μm, irrespective of alloy composition.

Larger differences in morphology were found in chips collected after finishing (Fig. 6). Alloys CW510L and CW732R showed quasi-continuous but finer chips, featuring curled shape. The CW614N alloy kept the tubular morphology of the interrupted chips, with some

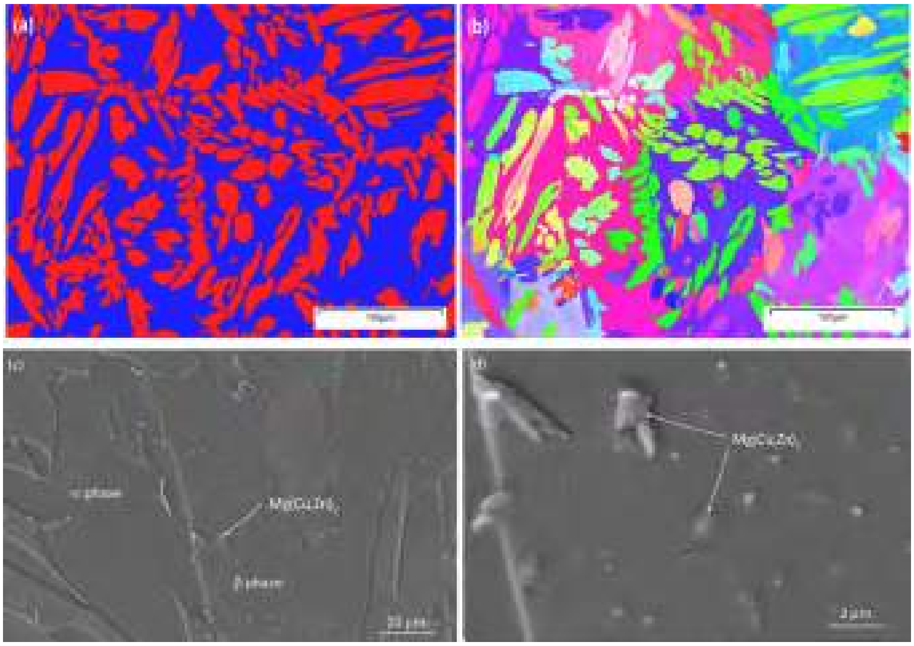

Fig. 3. Details of the microstructure of the CW732R alloy, detected by EBSD phase distribution (a) and inverse pole figures (b) and by higher magnification FE-SEM micrographs (c and d). In figure a, the red and blue domains correspond to α phase and β phase, respectively. (For interpretation of the references to colour in this figure legend, the reader is referred to the web version of this article.)

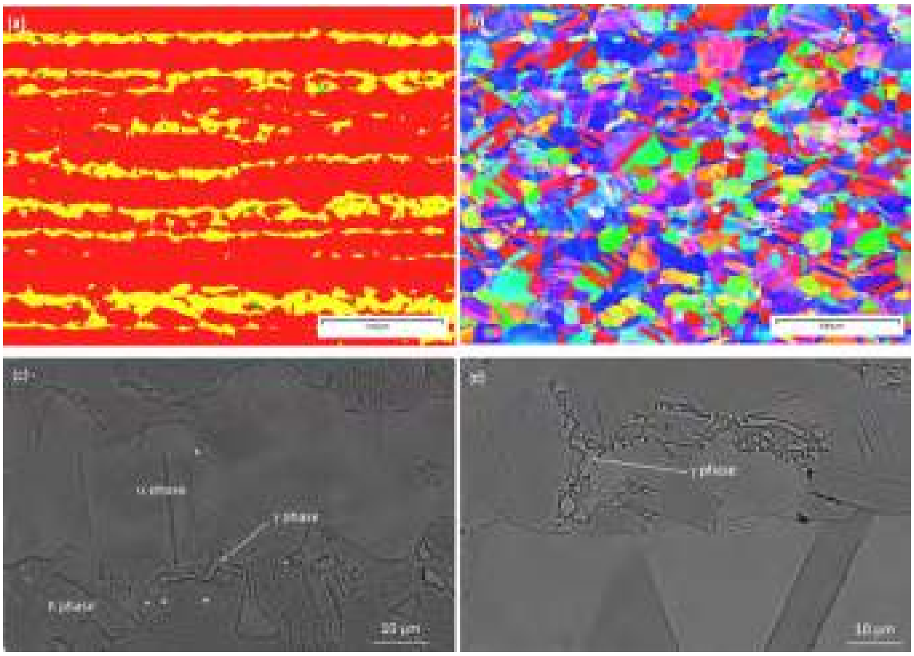

Fig. 4. Details about the microstructure of the CW724R alloy, detected by EBSD phase distribution (a) and inverse pole figures(b) and by higher magnification FE-SEM micrographs (c and d). In figure a, the red, yellow and green domains correspond to α phase, K phase and γ phase, respectively. (For interpretation of the references to colour in this figure legend, the reader is referred to the web version of this article.)

Table 3
Vickers' microhardness of the alloys investigated and abrasiveness estimated by eq. 2 and 3.

Alloy	HV_{2000}	HV_{10} α	HV_{10} β	HV_{10} K	HV_{25} γ	V_{β}	Vκ	Vγ	W_{ab}
CW510L / Cu42Zn	141,6 ± 5,0	133,8 ± 3,5	179,9 ± 1,2	–	–	0,50	–	–	165
CW614N / Cu39ZnPb3	138,9 ± 2,5	124,5 ± 5,5	171,4 ± 15,8	–.	–	0,23	–.	–	151
CW732R / CuZn41Mg	167,4 ± 3,7	130,2 ± 2,9	171,9 ± 6,6	–	–	0,55	–	–	190
CW724R / CuZn21Si3P	207,6 ± 5,4	168,7 ± 15,6	–	260,9 ± 22,5	440*	–	0,21	0,0047	233

* Data from[18].

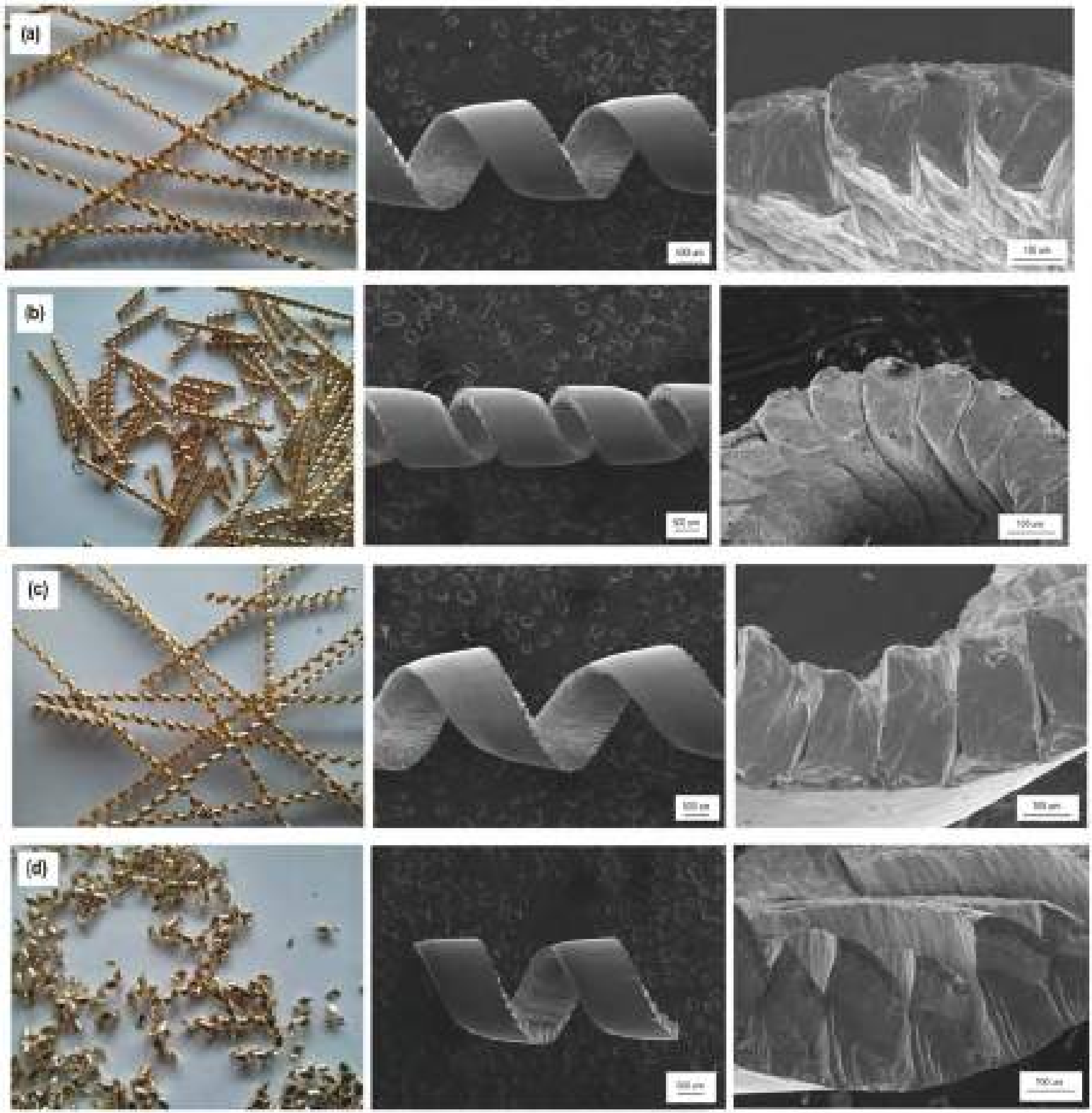

Fig. 5. Representative images of chip morphology produced according to roughing conditions for (a) CW510L alloy; (b) CW614N alloy, (c) CW732R alloy, (d) CW724R alloy.

similarities to those of the rough machining tests (see Fig. 5b). Finally, alloy CW724R shifted to a semi-continuous helical chip morphology.

At higher magnification, the saw-tooth appearance of the chips showing the distinct shear bands was still clearly visible, despite the shorter values of depth of cut and feed adopted. However, the average pitch distance revealed to be more alloy-dependent, increasing with the order: CW614N, CW732R, CW510L, CW724R.

The saw-tooth appearance of the chips, also identified as segmentation in the literature, highlighted in Figs. 5 and 6 is clearly confirmed by the images collected in Fig. 7 showing the sectioned chip samples created under roughing and finishing conditions. Such chip sections additionally allow observing the distorted microstructure and the main shear planes responsible for chip formation during cutting. The highest amount of shear deformation is observed at the chip bottom surfaces owing to the sliding action with friction against the tool rake face. The comparison among the materials machined under roughing conditions (Fig. 7, left-hand images) indicates that the CW724R alloy undergoes only limited shear along the tool-workpiece sliding interface, presumably due to its higher hardness, whereas all the other alloys exhibit extensive deformation of their microstructural constituents within a layer of approximately 20 μm beneath the exposed surface.

The morphology of the chips along the free surface opposite the tool–chip sliding interface provides insight into the chip-breaking mechanisms of the investigated alloys. Examination of the rough-machined, sectioned chips indicates that the CW510L and CW732R alloys (Fig. 7a and 7c, respectively) develop only limited visible shear bands, consistently with their predominantly continuous chip morphology. Deformation tends to localize at the boundaries between the α–β islands, although fracture of single-phase domains is not uncommon. In contrast, chip formation in the CW614N alloy (Fig. 7b) is strongly governed by the presence of the Pb globules, as expected. Fissures extending through the entire chip thickness, along with extensive cavitation, are clearly visible and are presumably initiated by the soft Pb particles during deformation. The Si-bearing CW724R alloy exhibits

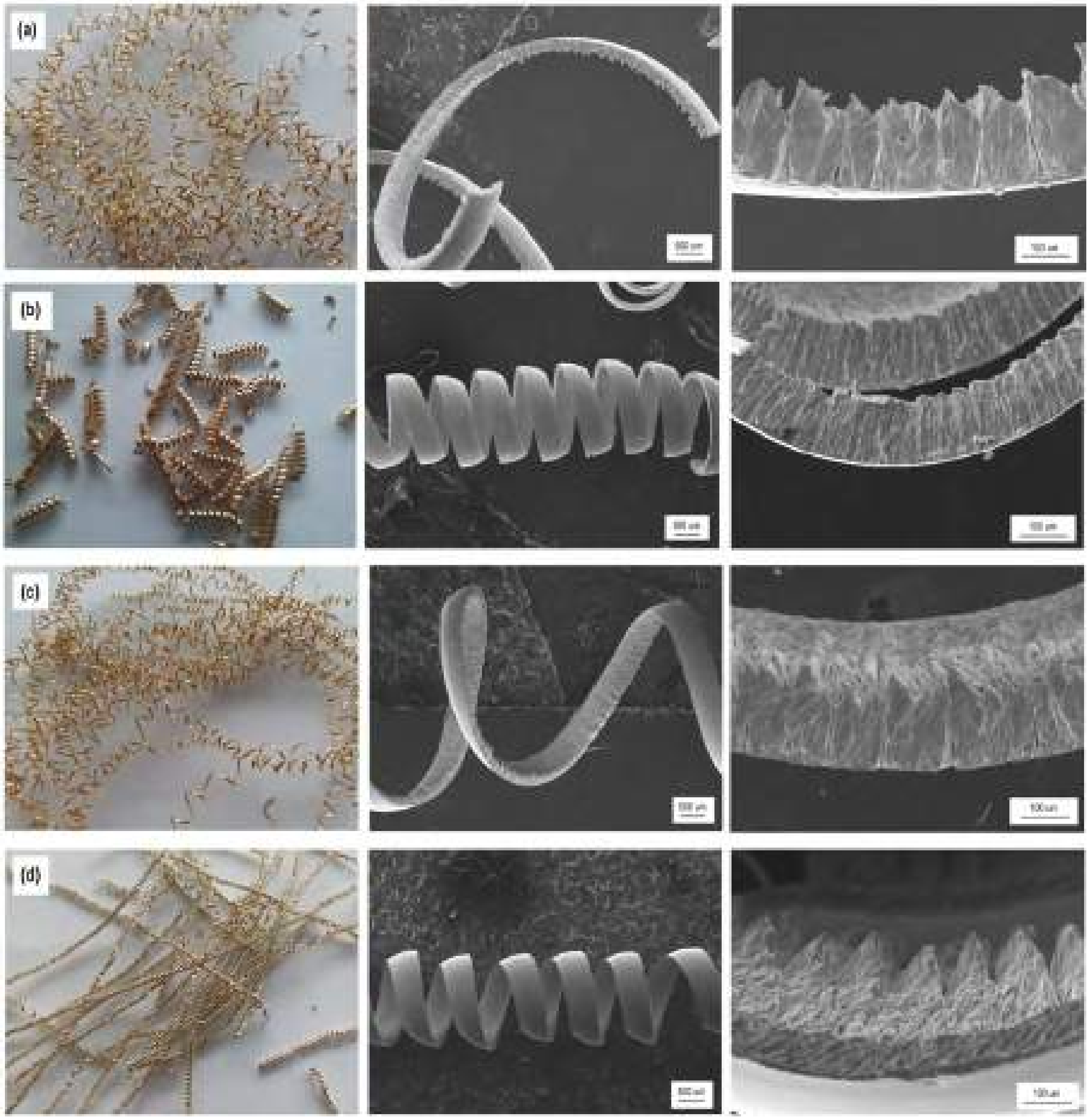

Fig. 6. Representative images of chip morphology produced according to finishing conditions for (a) CW510L alloy; (b) CW614N alloy, (c) CW732R alloy, (d) CW724R alloy.

deep cracks and localized shear bands traversing the microstructure along sharp, well-defined paths, without any marked indication of preferential propagation routes. This behaviour is likely dictated by the apparent brittleness of the alloy subjected to the stress field generated ahead of the deformation zone by the cutting tool. These observations can largely be extended also to the chips produced under fine-turning conditions. However, it is worth noting that the CW724R alloy displayed comparatively fewer cracks and reduced microstructural distortion within the deformed chips, consistent with the transition from a discontinuous to a continuous chip morphology (compare Fig. 5d and 6d).

Finally, Fig. 8 presents a set of representative images of the machined surfaces. As expected, the surface morphology is primarily governed by the selected machining parameters. The pitch distance between adjacent grooves corresponds to the applied feed rate, 0.2 and 0.1 mm/rev for roughing and finishing operations, respectively. At a finer scale, extensive smearing of the material exposed on the cut surface can be observed within the grooves. The longitudinal striations resulting from tool-tip imperfections are generally continuous. The only exception is alloy CW614N (Fig. 8b), which exhibits stepped and irregular features which are assumed to be connected to the repeated chip-breaking and separation events induced by the presence of the Pb particles. The surface roughness values measured along the bar axis after turning are reported in Table 4. For the alloys considered in this study, modifications in chemical composition and resulting microstructure appear to have a limited influence on surface roughness, whereas machining conditions play a dominant role. A possible exception is observed for the CW724R alloy, which exhibited slightly higher roughness under roughing conditions, likely due to the onset of mild vibrational effects during machining.

4. Discussion

Machining by chip removal remains one of the most widely

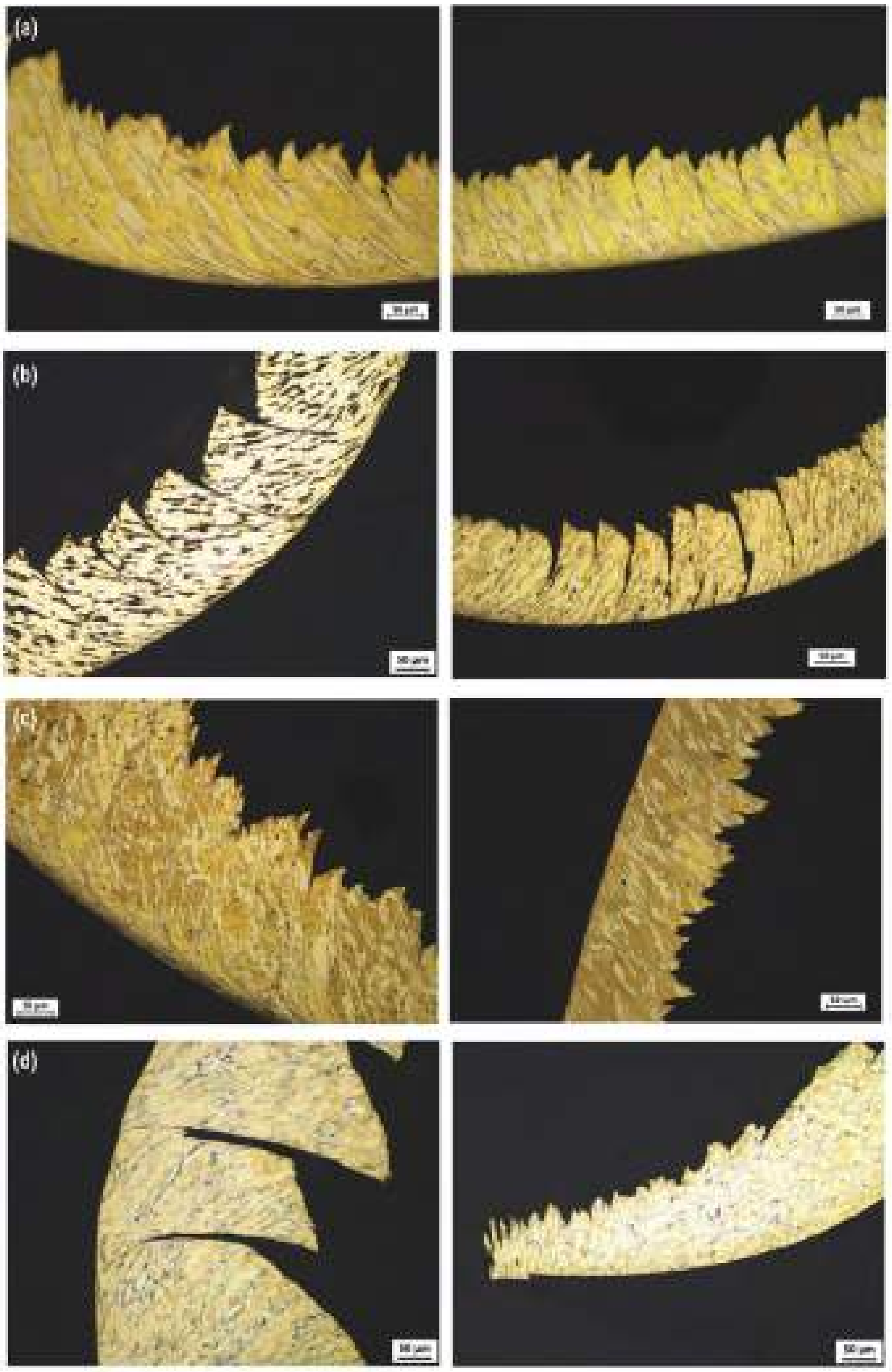

Fig. 7. Optical microscope images of sectioned chips produced according to roughing (left) and finishing (right) turning conditions for (a) CW510L alloy; (b) CW614N alloy, (c) CW732R alloy, (d) CW724R alloy.

employed methods for shaping mechanical components. It is well known that machining operations producing long, continuous chips are undesirable since such chips may entangle around the workpiece or tool, raising safety concerns for operators and potentially damaging the machined surfaces. Conversely, the extremely fine fragmented chips produced by lead-bearing alloys are also not ideal in industrial environments, as they may become airborne and be inhaled. In addition, fine chips tend to disperse and accumulate within machine components, leading to malfunctions, particularly in electrical systems and electronic circuits [15]. Therefore, strict control of chip morphology and fragmentation mechanisms via machining parameters, tool geometry, and alloy microstructure, is essential for ensuring efficient and safe manufacturing conditions. Both the literature and the results presented in this work clearly indicate that improved chip fragmentation in brasses is promoted by the severe shear strain developing in the cutting region, by the localization of deformation along specific shear bands induced by the dual-phase $\alpha + \beta$ microstructure, and by the presence of Pb globules, which introduce microstructural discontinuities that facilitate crack nucleation [15,18].

Alternative approaches in lead-free brasses rely on generating hard and brittle constituents capable of disrupting matrix continuity, thereby assisting chip breakage. In the alloys investigated here, this was achieved either through a dispersion-strengthening mechanism in CW732R, where $Mg(Cu,Zn)_2$ particles precipitate within the β phase, or through

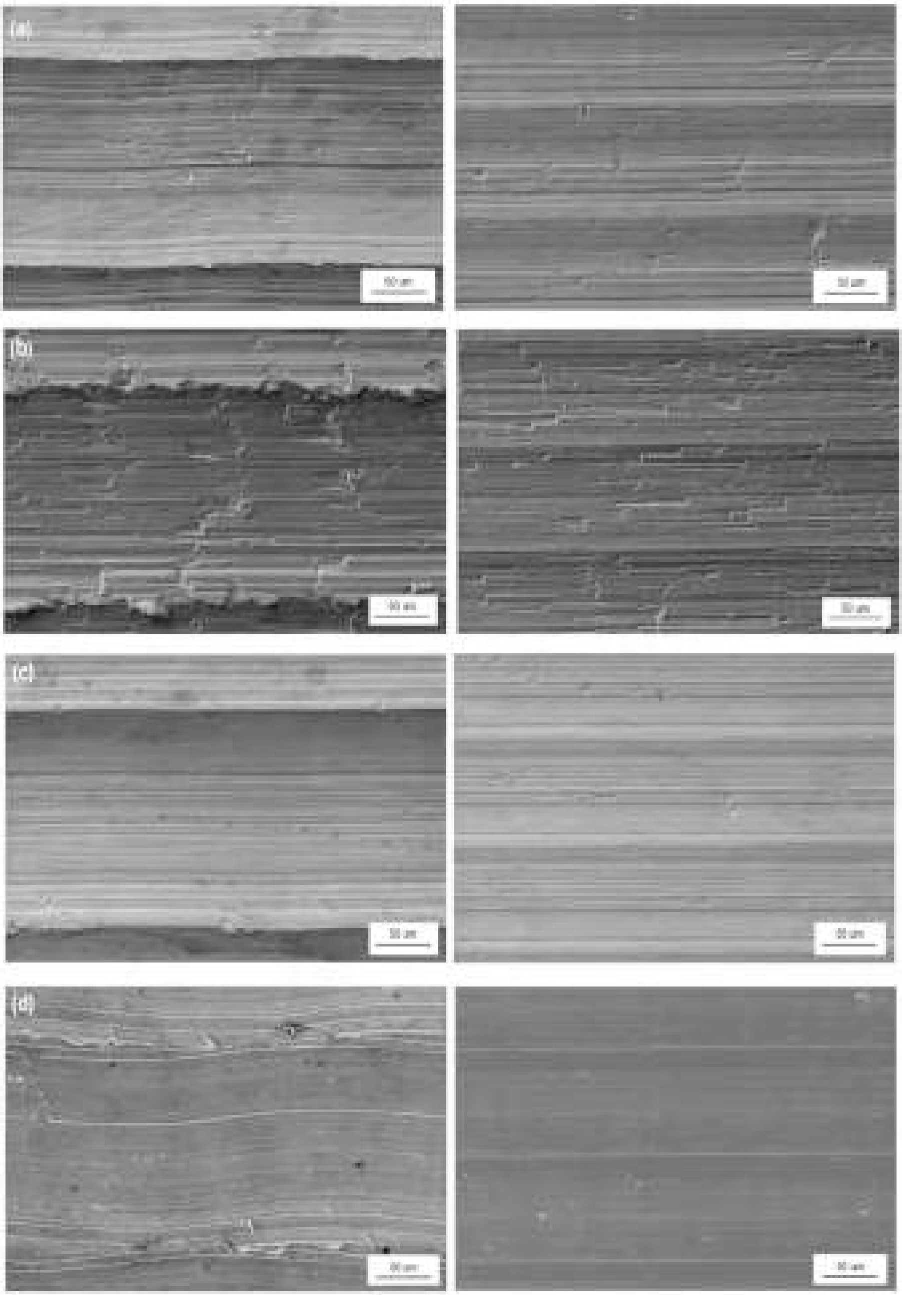

Fig. 8. Morphology of the machined surfaces of samples produced according to roughing (left) and finishing (right) turning conditions for (a) CW510L alloy; (b) CW614N alloy, (c) CW732R alloy, (d) CW724R alloy.

Table 4
Roughness values obtained in roughing and finishing turning on the tested alloys.

Alloy	Ra (μm) roughing	Ra (μm) finishing
CW510L / Cu42Zn	2.80	0.60
CW614N / Cu39ZnPb3	2.66	0.55
CW732R-DW / CuZn41Mg	2.63	0.64
CW724R / CuZn21Si3P	3.49	0.77

the addition of Si, which stabilizes the K and γ phases, both significantly harder and more brittle than the β phase in more conventional brasses.

Although machinability improvements are always dependent on specific machining conditions and parameters, the turning tests carried out in this study demonstrated that according to a chip control criterium, CW614N and CW724R alloys feature the formation of discontinuous and short chips. Chip morphology and fragmentation behavior can indeed be tailored by the aforementioned strategies. In particular, the brittle phases formed via Si addition were highly effective in promoting chip fragmentation during rough turning (Fig. 5d and 7d), whereas fine turning resulted in the formation of semi-continuous helical chips.

The Mg-bearing CW732R alloy, despite its higher hardness and larger fraction of the β phase (Table 2), exhibited a chip morphology broadly comparable to that of the CW510L alloy under the machining conditions adopted in this study. Nevertheless, previous investigations have shown that alternative turning regimes can significantly reduce cutting forces and promote the formation of short tubular chips [22,23].

Across all the investigated materials, a clear trend was observed: transitioning from finishing to roughing conditions (i.e., increasing feed and depth of cut) promoted the formation of more fragmented chips (see the comparison between Fig. 6 and Fig. 5). In line with this trend, it is reasonable to hypothesize that a further increase in the material removal rate—achieved by increasing feed and/or depth of cut—may also induce the expected transition toward shorter, more discontinuous chips in the CW732R alloy.

Therefore, the present results only appear to contradict the promising machinability reported for similar Mg-bearing brasses in the literature, further confirming that machinability assessments are strongly dependent on the specific processing conditions. In this context, Seuß and co-authors investigated the machinability and other relevant properties of a Mg-bearing CW732R alloy and reported good machinability, even without or with only minor adjustments to the cutting parameters. For completeness, they also noted that, in grooving operations, the use of appropriate tools equipped with chip-breakers is advisable [23]. Overall, these findings confirm that the microstructural design of free-machining alloys must be closely tailored to the specific chip-removal technology and machining parameters employed. In principle, the microstructure-governed shear mechanisms that rule chip formation are expected to qualitatively hold across all machining processes based on similar chip-generation architectures (e.g., turning, drilling, and milling). Turning is the process that most closely approximates the ideal conditions of orthogonal cutting. For this reason, it was selected as the machining technology for the present investigation. However, it is well established that even minor variations in tool geometry, cutting parameters, lubrication conditions, and system stiffness can lead to significant quantitative differences in machining performance. In the case of milling, the most important distinction lies in its discontinuous nature, which inherently leads to chip segmentation. This, together with the resulting differences in thermal behaviour, makes it more complex to predict the response of the tested alloys. As for drilling, the process involves a different geometry and more complex thermal conditions, further complicating the quantitative extension of the obtained predictions.

Considering surface topology, Fig. 8 proposes a comparison of the surface aspect left after machining of the investigated alloys. The representative SEM images of the machined alloys highlight a comparable macroscopic texture of the surfaces, as ruled mainly by the machining parameters. A further interesting aspect specific for the machined CW614N alloy, consists in the presence of periodic striations or steps perpendicularly oriented to the kerf created by the tool (see Fig. 8b). These striations are supposed to be generated by the abrupt chip fracture induced by the dispersion of Pb particles. The assumption is also supported by the comparable distance among these striations and the shear band spacing depicted in Fig. 7b. Somehow, the good machinability of this alloy is related to the chip breakage that also leaves a signature on the surface.

Finally, a side effect of introducing hard constituents in these lead-free alloys is the increased abrasiveness toward cutting tools. The abrasiveness estimates reported in Table 3 confirm that CW732R alloy and CW724R alloy are expected to impose a greater demand on tool wear resistance. On the positive side, these hard constituents also contribute to the strengthening of the alloys. Although a detailed analysis of mechanical properties is beyond the scope of the present work, several studies have reported strength data of lead-free brasses, for example [12,13,17,18] for Si-bearing alloys and [21,23] for Mg-bearing ones. All published data consistently indicate increased ultimate tensile strength and yield strength compared with both the standard CW510L alloy and the lead-bearing CW614N alloy, with only a modest reduction in fracture elongation.

5. Conclusions

Lead-free brasses with enhanced machinability belonging to the Cu–Zn–Si (CW724R) and Cu–Zn–Mg (CW732R) alloy systems were investigated and compared with the more conventional CuZn42 (CW510L) and CuZn39Pb3 (CW614N) brasses. The analysis of the microstructure-related mechanisms responsible for the machinability of these alloys led to the following conclusions.

- Thermo-Calc simulations combined with microstructural investigations revealed that in CW510L and CW614N alloys the primary β phase forms upon solidification, followed by partial solid-state transformation into the FCC α phase. In the lead-bearing CW614N alloy, the low-melting Pb separates from the Cu-rich matrix during solidification and enters the solid state at temperatures as low as 327.5°C. The Mg-bearing CW732R alloy develops a similar α + β microstructure, with additional precipitation of sub-micrometric $Mg(Cu,Zn)_2$ particles within the β grains. In the CW724R alloy, the combined effects of Si and Zn suppress the formation of the β phase in favour of the K phase (nominal stoichiometry Cu_8Zn_2Si), along with limited fractions of γ phase segregated at grain boundaries.
- The introduction of Mg- and Si-bearing phases in CW732R and CW724R alloy, respectively, increases the hardness contrast among microstructural constituents, which is assumed to enhance machinability by promoting chip discontinuity. An abrasiveness parameter toward cutting tools was estimated for these multiphase alloys, suggesting a moderate increase in expected tool wear compared with the reference lead-free alloy.
- Chip morphology analyses under both roughing and finishing conditions elucidated the dominant chip-formation mechanisms. As expected, the reference lead-free CW510L alloy produced semi-continuous chips during rough turning and continuous curled chips during finish turning. In contrast, the benchmark lead-bearing CW614N alloy consistently generated tightly curled, fragmented tubular chips. The Mg-bearing CW732R alloy, despite a higher hardness of the β phase due to submicrometric precipitates exhibited semi-continuous chips under the rough turning and continuous curled chips under the finish turning conditions here investigated. Finally, the CW724R alloy, which exhibited the largest hardness increase due to the presence of Si-containing phases, produced discontinuous chips during rough turning and semi-continuous chips during finish turning.
- Metallographic examination of chip cross-sections provided further evidence of the underlying chip-formation mechanisms. In CW510L and CW732R alloys limited evidence of shear bands was noted, consistently with their predominantly continuous chip morphology. Deformation localized at the boundaries between the α–β islands, although fracture of single-phase domains was not uncommon. In CW614N alloy, chip formation was strongly influenced by fissures initiating at Pb globules and propagating across the entire chip thickness. The Si-bearing CW724R alloy exhibited segmented chips with deep cracks and localized shear bands crossing the microstructure along sharp and well-defined paths, without any clear indication of preferred propagation routes.

Funding sources

No funding has been received by the author for the published research work.

CRediT authorship contribution statement

Erfan Sharghivand: Investigation, Data curation. **Luca Bazzana:** Methodology, Conceptualization. **Antonio Costetti:** Investigation, Data curation. **Nino Mori:** Methodology, Conceptualization. **Massimiliano Annoni:** Writing – original draft, Methodology, Investigation. **Maurizio Vedani:** Writing – review & editing, Writing – original draft, Methodology, Conceptualization.

Declaration of competing interest

The authors declare that they have no known competing financial interests or personal relationships that could have appeared to influence the work reported in this paper.

Acknowledgements

The authors acknowledge the valuable contributions of R.M. Ishola, L. Rovatti, and M. Pizzi for their contribution to the experimental work.

Data availability

Data will be made available on request.

References

[1] P. Stavroulakis, A.I. Toulfatzis, G.A. Pantazopoulos, A.S. Paipetis, Machinable Leaded and Eco-Friendly Brass Alloys for High Performance Manufacturing Processes: a critical Review, Metals 12 (2022) 1–31, https://doi.org/10.3390/met12020246.

[2] J. Johansson, P. Alm, R.M. Saoubi, P. Malmberg, J.E. Ståhl, V. Bushlya, On the function of lead (Pb) in machining brass alloys, Int. J. Adv. Manuf. Techn. 120 (2022) 7263–7275, https://doi.org/10.1007/s00170-022-09205-0.

[3] P. García, S. Rivera, M. Palacios, J. Belzunce, Comparative study of the parameters influencing the machinability of leaded brasses, Eng. Fail. an. 17 (2010) 771–776, https://doi.org/10.1016/j.engfailanal.2009.08.012.

[4] G. Pantazopoulos, Leaded Brass Rods C 38500 for Automatic Machining Operations: a Technical Report, J. Mater. Eng. Perf. 11 (2002) 402–407, https://doi.org/10.1361/105994902770343926.

[5] A.I. Toulfatzis, G.J. Besseris, G.A. Pantazopoulos, C. Stergiou, Characterization and comparative machinability investigation of extruded and drawn copper alloys using non-parametric multi-response optimization and orthogonal arrays Int, J. Adv. Manuf. Techn. 57 (2011) 811–826, https://doi.org/10.1007/s00170-011-3319-1.

[6] K.W. Siu, J.C.M. Kwok, A.H.W. Ngan, Thermo-mechanical processing of brass components for potable-water usage increases risks of Pb leaching, Water Res. 186 (2020) 116414, https://doi.org/10.1016/j.watres.2020.116414.

[7] S. Triantafyllidou, J. Parks, M. Edwards, Lead Particles in Potable Water, J. Am. Water Works Ass. 99 (2007) 107–117, https://doi.org/10.1002/j.1551-8833.2007.tb07959.x.

[8] Use of Lead-Free Pipes, Fittings, Fixtures, Solder, and Flux for Drinking Water. https://www.epa.gov/sdwa/use-lead-free-pipes-fittings-fixtures-solder-and-flux-drinking-water. 2025 (accessed 03 February 2026).

[9] P. Suksongkarm, S. Rojananan, S. Rojananan, Bismuth formation in lead-free Cu-Zn-Si yellow brass with various bismuth-tin alloy additions, Mater. Trans. 59 (2018) 1747–1752, https://doi.org/10.2320/matertrans.M2018081.

[10] P. Suksongkarm, S. Rojananan, S. Rojananan, Using Recycled Bismuth-Tin Solder in Novel Machinable Lead-Free Brass, Mater. Trans. 58 (2017) 1754–1760, https://doi.org/10.2320/matertrans.M2017227.l.

[11] H. Atsumi, H. Imai, S. Li, K. Kondoh, Y. Kousaka, A. Kojima, The effect of Solid Solutionizing Ti Element on Microstructural and Mechanical Properties of Extruded Cu-40Zn-Ti Ternary Alloy, Trans. JWRI 40 (2011) 67–71. https://doi.org/10.18910/10014.

[12] F. Schultheiss, D. Johansson, V. Bushlya, J. Zhou, K. Nilsson, J.E. Ståhl, Comparative study on the machinability of lead-free brass, J. Clean. Prod. 149 (2017) 366–377, https://doi.org/10.1016/j.jclepro.2017.02.098.

[13] K. Suzaki, H. Goto, K. Oishi, Development of Lead-Free High-Strength Copper Alloy, Mater. Trans. 61 (2020) 1684–1688, https://doi.org/10.2320/matertrans.MT-M2020045.

[14] X. Zhang, C. Ma, S. Li, D. Pan, F. Zheng, Interface design of lead-free free-cutting titanium reinforced graphite brass composites and its effect on mechanical properties and cutting performance, Mater. Sci. Eng. A 774 (2020) 13890, https://doi.org/10.1016/j.msea.2020.138909.

[15] C. Nobel, F. Klocke, D. Lung, S. Wolf, Machinability Enhancement of Lead-Free Brass Alloys, Proc. CIRP 14 (2014) 95–100, https://doi.org/10.1016/j.procir.2014.03.018.

[16] Ö. Semih, A. Recep, Investigation of microstructure, machinability, and mechanical properties of new-generation hybrid lead-free brass alloys, High Temp. Mater. Proc. 42 (2023) 20220263, https://doi.org/10.1515/htmp-2022-0263.

[17] M.A. Taha, N.A. El-Mahallawy, R.M. Hammouda, T.M. Moussa, M.H. Gheith, Machinability characteristics of lead free-silicon brass alloys as correlated with microstructure and mechanical properties, Ain Shams Eng. J. 3 (2012) 383–392, https://doi.org/10.1016/j.asej.2012.05.004.

[18] C. Yang, Z. Ding, Q.C. Tao, L. Liang, Y.F. Ding, W.W. Zhang, Q.L. Zhu, High-strength and free-cutting silicon brasses designed via the zinc equivalent rule, Mater. Sci. Eng. A 723 (2018) 296–305, https://doi.org/10.1016/j.msea.2018.03.055.

[19] J. Choucri, F. Zanotto, V. Grassi, A. Balbo, M.E. Touhami, I. Mansouri, C. Monticelli, Corrosion Behavior of different brass alloys for drinking water distribution systems, Metals 9 (2019) 649, https://doi.org/10.3390/met9060649.

[20] M.A. Taha, N. A. E-Mahallawy, T.M. Mousa, R. M. Hamouda, A. F. A. G. Yousef., Microstructure and castability of lead-free silicon brass alloys, Mater. Sci. Eng. Techn. 43 (2012) 699–704, https://doi.org/10.1002/mawe.201200932.

[21] H. Atsumi, H. Imai, S. Li, K. Kondoh, Y. Kousaka, A. Kojima, Fabrication and properties of high-strength extruded brass using elemental mixture of Cu-40% Zn alloy powder and Mg particle, Mater. Chem. Phys. 135 (2012) 554–562, https://doi.org/10.1016/j.matchemphys.2012.05.025.

[22] M. Adineh, H. Doostmohammadi, Microstructure, mechanical properties and machinability of Cu–Zn–Mg and Cu–Zn–Sb brass alloys, Mater. Sci. Techn. 35 (2019) 1504–1514, https://doi.org/10.1080/02670836.2019.1630089.

[23] F. Seuß, P. Feldner, H. Ricken, A. Dehnelt. eZeebrass – A novel lead-free standard machining brass. In: Proceedings of Copper Alloys 2024 – Scientific Conference on Copper Materials, Kupferverband e.V., Stockholm, Sweden, 8–9 October 2024.

[24] D. Suksongkarm, S. Rojananan, S. Rojananan, Microstructure and Hardness of Cu-Zn-Si-Al-Sn Brasses with Antimony Addition, Adv. Mater. Res. 802 (2013) 179–183, https://doi.org/10.4028/www.scientific.net/AMR.802.179.